Detection of the gravitational lens magnifying a type Ia supernova.

AUTHOR(S):

Quimby, Robert M; Oguri, Masamune; More, Anupreeta; More, Surhud; Moriya, Takashi J; Werner, Marcus C; Tanaka, Masayuki; ... Bersten, Melina C; Maeda, Keiichi; Nomoto, Ken'ichi

CITATION:

Quimby, Robert M ...[et al]. Detection of the gravitational lens magnifying a type Ia supernova.. Science 2014, 344(6182): 396-399

ISSUE DATE:

2014-04-25

URL:

http://hdl.handle.net/2433/186162

Detection of the Gravitational Lens Magnifying a Type Ia Supernova

Robert M. Quimby,[1*] Masamune Oguri,[1,2] Anupreeta More,[1] Surhud More,[1] Takashi J. Moriya,[3,4] Marcus C. Werner,[1] Masayuki Tanaka,[5] Gaston Folatelli,[1] Melina C. Bersten,[1] Keiichi Maeda,[6] and Ken'ichi Nomoto,[1]

[1]Kavli Institute for the Physics and Mathematics of the Universe (WPI), Todai Institutes for Advanced Study, The University of Tokyo, 5-1-5 Kashiwanoha, Kashiwa-shi, Chiba, 277-8583, Japan
[2]Department of Physics, The University of Tokyo, Tokyo 113-0033, Japan
[3]Argelander Institute for Astronomy, University of Bonn Auf dem Hügel 71, D-53121 Bonn, Germany
[4] Research Center for the Early Universe, Graduate School of Science University of Tokyo, Hongo 7-3-1, Bunkyo, Tokyo 113-0033, Japan
[5] National Astronomical Observatory of Japan 2-21-1 Osawa, Mitaka, Tokyo 181-8588, JAPAN
[6] Department of Astronomy, Kyoto University, Kitashirakawa-Oiwake-cho Sakyo-ku, Kyoto 606-8502, Japan

*To whom correspondence should be addressed; E-mail: robert.quimby@ipmu.jp.

Objects of known brightness, like Type Ia supernovae (SNIa), can be used to measure distances. If a massive object warps spacetime to form multiple images of a background SNIa, a direct test of cosmic expansion is also possible. However, these lensing events must first be distinguished from other rare phenomena. Recently, a supernova was found to shine much brighter than normal for its distance, which resulted in a debate: was it a new type of superluminous

supernova or a normal SNIa magnified by a hidden gravitational lens? Here we report that a spectrum obtained after the supernova faded away shows the presence of a foreground galaxy–the first found to strongly magnify a SNIa. We discuss how more lensed SNIa may be found than previously predicted.

A peculiar supernova, PS1-10afx, was discovered by the Panoramic Survey Telescope & Rapid Response System 1 (Pan-STARRS1) on 2010 August 31 (UT) (*1*). The unusually red color of the object spurred the Pan-STARRS1 team to conduct an array of follow-up observations including optical and near infrared spectroscopy, which yielded a redshift of $z = 1.39$. Combined with relatively bright photometric detections, this redshift would imply a peak luminosity of 4×10^{44} erg s^{-1}, which is 400 times brighter than the typical core-collapse supernova. A rare class of superluminous supernovae (SLSN) (*2*) have shown similarly high bolometric outputs, but PS1-10afx distinguishes itself from all other SLSN on two important counts: PS1-10afx is much redder (cooler) and evolved much faster than any SLSN. A generic feature of SLSN models (*3–9*) is that they employ high temperatures and/or large photospheric radii to generate high luminosities (recalling that $L \propto T^4 R^2$). The observations of PS1-10afx do not fit with these models, suggesting that if it is a SLSN, it is in a class of its own.

An alternate hypothesis (*10*) is that PS1-10afx is actually a regular Type Ia supernova (SNIa) with a normal luminosity, but its apparent brightness has been magnified by a gravitational lens. Spectra of PS1-10afx are well fit by normal SNIa templates, as are the colors and light curve shapes. However, normal SNIa exhibit a tight relation between the widths of their light curves and their peak luminosities (*11–14*), and PS1-10afx appears 30 times brighter than expected according to this relation. Such a large magnification of brightness can only occur naturally from strong gravitational lensing, whereby the light emanating from the supernova is bent to form an Einstein-Chwolson ring, or several discrete magnified images (typically two or four) if the alignment is not axisymmetric. Pan-STARRS1 has surveyed sufficient volume to expect

such a chance alignment (*15, 16*) and it is possible that the angular extent of the lensed images was simply too small to be resolved by the observations available. However, for this hypothesis to be confirmed, we must explain why the existing observations give such conclusive photometric and spectroscopic evidence for the presence of the supernova's host galaxy, but the same observations fail to obviously indicate the presence of a foreground lens.

We used the Keck-I telescope with the Low-Resolution Imaging Spectrograph (LRIS) (*17*) with the upgraded red channel (*18*) to observe the host galaxy and any foreground objects at the sky position of PS1-10afx on 2013 September 7 (see Fig. S1) (*16*). As illustrated in figure 1, there are two narrow emission features that persist at the location of PS1-10afx now that the supernova itself has faded away. The [O II] emission doublet ($\lambda\lambda = 3726.1, 3728.8$ Å in the rest frame) from the host galaxy previously identified (*1*) is clearly recovered (Fig. S2), but we additionally detected a second emission line at about 7890 Å. Because there are no strong emission lines expected from the host at this wavelength (∼3300 Å in the host frame), this detection suggests the presence of a second object coincident with PS1-10afx.

The most probable identification for the 7890 Å feature is [O II] at $z = 1.1168 \pm 0.0001$. At this redshift, other strong emission lines such as H-beta or [O III] would lie outside of our wavelength coverage. However, as depicted in figure 1, we detected a Mg II absorption doublet ($\lambda\lambda = 2795.5, 2802.7$ Å in the rest frame) at $z = 1.1165 \pm 0.0001$. Blueshifted absorption outflows are typical of star-forming galaxies (*19*), so this estimate is compatible with that derived from the emission lines. We also identify possible Mg I ($\lambda = 2853.0$) and Fe II ($\lambda = 2344.2, 2373.7, 2382.8, 2586.7, 2600.2$) lines with a matching redshift. Given these identifications and the extended nature of the emission (see Fig. S3), it is clear that the second object is a galaxy lying in front of PS1-10afx and its host. Indeed, the near maximum light spectra of PS1-10afx (*1*) show what could be Ca II absorption from this foreground galaxy (Fig. 1).

With its redshift secure, we next checked whether the foreground galaxy can satisfy the lens

requirements of PS1-10afx (*10*). To do this, we derived a stellar mass for the foreground galaxy and used an empirical relation between stellar mass and 1-D velocity dispersion as explained below. We fitted a set of single stellar population (SSP) models to the combined spectra to measure the stellar masses of the host and foreground galaxies (see Figs. 2 and S4) (*16*). The best-fit SSP combination was a $\sim$1 Gyr old foreground galaxy with a stellar mass of $(9 \pm 2) \times 10^9\,\mathrm{M}_\odot$ and a more distant host galaxy with $(7 \pm 1) \times 10^9\,\mathrm{M}_\odot$ and a younger ($\sim$0.1 Gyr) population. The extinction in the foreground galaxy is consistent with zero ($A_V = 0.28^{+0.48}_{-0.28}$), but the host galaxy requires significant reddening ($A_V = 1.62 \pm 0.18$).

Stellar mass contributes only a fraction of a galaxy's total mass, which is usually dominated by dark matter. The ratio of these masses varies from galaxy to galaxy, but they are strongly correlated. Using the stellar-mass-to-velocity-dispersion relation measured from the SDSS DR7 spectroscopic sample (*20, 21*) (see Fig. S5), we inferred a probability distribution for the foreground galaxy's velocity dispersion (*16*). We then used this as input to a Monte Carlo simulation from which we derived the posterior distributions for the lens parameters (Fig. 3). We find that the redshift and mass of the foreground galaxy make it fully consistent with a gravitational lens that is capable of satisfying the magnification, image separation limits, and time delay constraints of PS1-10afx (*10*). We thus concluded that PS1-10afx is not a superluminous supernova but a normal SNIa magnified by a strong gravitational lens at $z = 1.1168$.

Our new data further explain why the lensing galaxy was not evident in prior observations. Even though the host galaxy is slightly less massive, more extinguished, and farther away than the lensing galaxy, it harbors a younger stellar population that shines more brightly per unit mass. Because of this, the foreground object is only comparable in brightness to the host over a narrow range of wavelengths longer than the lensing galaxy's 4000 Å break but shorter than the host's. This makes it difficult to see the light from the lens galaxy over the glare from the host galaxy.

The lack of multiple images or signs of time delay from PS1-10afx can also be explained from our Monte Carlo simulations. The high total magnification of PS1-10afx is best recovered from alignments that produce four images (79% probability of a "quad" system), but the maximum separation between the different multiple images is small ($\Delta\theta < 0.12''$ at 95% confidence) and the maximum phase delay is short ($\Delta t < 1.3$ day at 95% confidence). The available observations of PS1-10afx are thus likely insufficient to resolve any effects from the gravitational lensing other than its magnification.

In the future, high angular resolution imaging enabled by adaptive optics (AO) or space-based resources like the Hubble Space Telescope (*HST*) could be used to spatially resolve the multiple images of gravitational lensed SNIa like PS1-10afx. This would not only provide immediate confirmation that gravitational lensing is at play, but it would also provide important constraints on the nature of the lens. In theory, multiple epochs of high resolution imaging could be used to measure the time delay between each image and the magnification factors for each. Such observations could yield strong constraints on cosmic expansion.

Because the universe is expanding, the path lengths of the more delayed images will be stretched more by cosmic expansion, and the magnitude of this delay is directly tied to the Hubble parameter (*22*). However, the time delay is also dependent on the mass density profile of the lens, which will be dictated by unobservable dark matter. For objects of known brightness, like SNIa, we can use the readily measurable magnification to break this degeneracy (*23*). As is likely the case for PS1-10afx, spectra taken near maximum light can reveal not only the redshift of the supernova but, using absorption line spectroscopy, the redshift and velocity dispersion of the lens as well. (Note that at maximum light, the resolving power available from Keck/LRIS may have been sufficient to resolve the Ca II K line from the lens, but the signal-to-noise ratio and resolution of the available observations is too low: $\sigma < 125\,\mathrm{km\ s^{-1}}$ at 95% confidence.) Thus, future discoveries of gravitationally lensed SNIa may be used to make a direct and precise

measurement of the Hubble constant, but only if the needed follow-up observations commence in a timely manner.

To begin follow-up observations of lensed SNIa candidates while they are still on the rise (needed for accurate delay time measurements) or near maximum light (the optimal phase for absorption line spectroscopy), an efficient vetting process must be employed to eliminate the non-lensed supernovae that out number lensed SNIa by a few thousand to one. A means to accomplish this feat was demonstrated by the selection of PS1-10afx for follow-up by the Pan-STARRS1 team – they were first motivated to examine PS1-10afx based on its unusually red color (*1*). In figure 4 we show a color-magnitude diagram for observed supernovae (*16*). PS1-10afx showed a color near maximum light of $r-i \sim 1.7$ whereas un-lensed supernovae brighter than the Pan-STARRS1 detection limits have $r - i < 0.5$. (Note that quiescent galaxy light is removed from these measurements using pre-supernova images). Since the lensing probability increases with redshift and, for a given sky area, the number of supernovae also increases with redshift (because of both rates and increased volume), the majority of lensed SNIa expected from a flux limited survey will be high redshift events that will typically appear much redder than the more nearby population of un-lensed supernovae. We thus propose that selecting supernovae with colors redder that the bold line in figure 4 (for a given i-band magnitude) during their rise to peak may be an effective way to identify lensed supernovae. This will bypass the need to detect multiple, resolved images and will thus increase the expected number of lensed SN Ia from future surveys by a factor of 5 over traditional selection techniques.

The large magnification and relatively low-mass lens galaxy of PS1-10afx may prove typical of gravitationally lensed SNIa that will be discovered by future, flux-limited surveys given selection bias: brighter objects are easier to detect, and unresolved images formed by a low-mas lens effectively make a single, brighter object (*16*) (see Fig. S6). Alternatively, the lens mass and high magnification of PS1-10afx may indicate a problem with our understanding of

the starlight to dark matter connection in the early universe. Further studies of this system are thus warranted. A multi-wavelength, high-angular-resolution study of the lens and host galaxies with *HST*, ground based AO, and the Atacama Large Millimeter/submillimeter Array (ALMA) could further constrain the lensing model and provide an important reference for future studies of gravitationally lensed SNIa.

References and Notes

1. R. Chornock, *et al.*, *ApJ* **767**, 162 (2013).
2. A. Gal-Yam, *Science* **337**, 927 (2012).
3. G. Rakavy, G. Shaviv, Z. Zinamon, *ApJ* **150**, 131 (1967).
4. Z. Barkat, G. Rakavy, N. Sack, *Physical Review Letters* **18**, 379 (1967).
5. S. E. Woosley, S. Blinnikov, A. Heger, *Nature* **450**, 390 (2007).
6. S. E. Woosley, *ApJ* **719**, L204 (2010).
7. D. Kasen, L. Bildsten, *ApJ* **717**, 245 (2010).
8. R. A. Chevalier, C. M. Irwin, *ApJ* **729**, L6 (2011).
9. T. J. Moriya, *et al.*, *MNRAS* **428**, 1020 (2013).
10. R. M. Quimby, *et al.*, *ApJ* **768**, L20 (2013).
11. M. M. Phillips, *et al.*, *AJ* **118**, 1766 (1999).
12. S. Jha, A. G. Riess, R. P. Kirshner, *ApJ* **659**, 122 (2007).
13. M. Hicken, *et al.*, *ApJ* **700**, 1097 (2009).

14. M. Sullivan, *et al.*, *MNRAS* **406**, 782 (2010).

15. M. Oguri, P. J. Marshall, *MNRAS* **405**, 2579 (2010).

16. Additional information is available in the supplementary materials.

17. J. B. Oke, *et al.*, *PASP* **107**, 375 (1995).

18. C. Rockosi, *et al.*, *Society of Photo-Optical Instrumentation Engineers (SPIE) Conference Series* (2010), vol. 7735 of *Society of Photo-Optical Instrumentation Engineers (SPIE) Conference Series*.

19. D. K. Erb, A. M. Quider, A. L. Henry, C. L. Martin, *ApJ* **759**, 26 (2012).

20. G. Kauffmann, *et al.*, *MNRAS* **341**, 33 (2003).

21. M. R. Blanton, *et al.*, *AJ* **129**, 2562 (2005).

22. S. Refsdal, *MNRAS* **128**, 307 (1964).

23. M. Oguri, Y. Kawano, *MNRAS* **338**, L25 (2003).

24. A. V. Filippenko, *PASP* **94**, 715 (1982).

25. R. W. Hanuschik, *A&A* **407**, 1157 (2003).

26. IRAF is distributed by the National Optical Astronomy Observatory, which is operated by the Association of Universities for Research in Astronomy (AURA) under cooperative agreement with the National Science Foundation.

27. C. Buton, *et al.*, *A&A* **549**, A8 (2013).

28. P. G. van Dokkum, *PASP* **113**, 1420 (2001).

29. D. D. Kelson, *PASP* **115**, 688 (2003).

30. V. C. Rubin, W. K. J. Ford, N. . Thonnard, *ApJ* **238**, 471 (1980).

31. M. Cappellari, E. Emsellem, *PASP* **116**, 138 (2004).

32. G. Bruzual, S. Charlot, *MNRAS* **344**, 1000 (2003).

33. S. D. J. Gwyn, *PASP* **120**, 212 (2008).

34. B. C. Kelly, *ApJ* **665**, 1489 (2007).

35. M. Oguri, *PASJ* **62**, 1017 (2010).

36. R. Bezanson, *et al.*, *ApJ* **737**, L31 (2011).

37. W. Li, *et al.*, *MNRAS* **412**, 1441 (2011).

38. See http://supernova.lbl.gov/∼nugent/nugent_templates.html.

39. E. Y. Hsiao, *et al.*, *ApJ* **663**, 1187 (2007).

40. O. Graur, *et al.*, *MNRAS* **417**, 916 (2011).

41. M. Bernardi, *et al.*, *MNRAS* **404**, 2087 (2010).

42. J. Guy, *et al.*, *A&A* **523**, A7 (2010).

43. S. Belli, A. B. Newman, R. S. Ellis, *ArXiv e-prints* (2013).

44. **Acknowledgments:** This work was supported in part by the Kakenhi Grant-in-Aid for Young Scientists (B)(24740118) from the Japan Society for the Promotion of Science, the World Premier International Research Center Initiative, MEXT, Japan, the FIRST program, "Subaru Measurements of Images and Redshifts (SuMIRe)," and by the Japan Society for

the Promotion of Science Research Fellowship for Young Scientists (23-5929). The data presented herein were obtained at the W.M. Keck Observatory, which is operated as a scientific partnership among the California Institute of Technology, the University of California and the National Aeronautics and Space Administration. The Observatory was made possible by the generous financial support of the W.M. Keck Foundation. The data presented in this paper are available from the Weizmann Interactive Supernova Data Repository (www.weizmann.ac.il/astrophysics/wiserep).

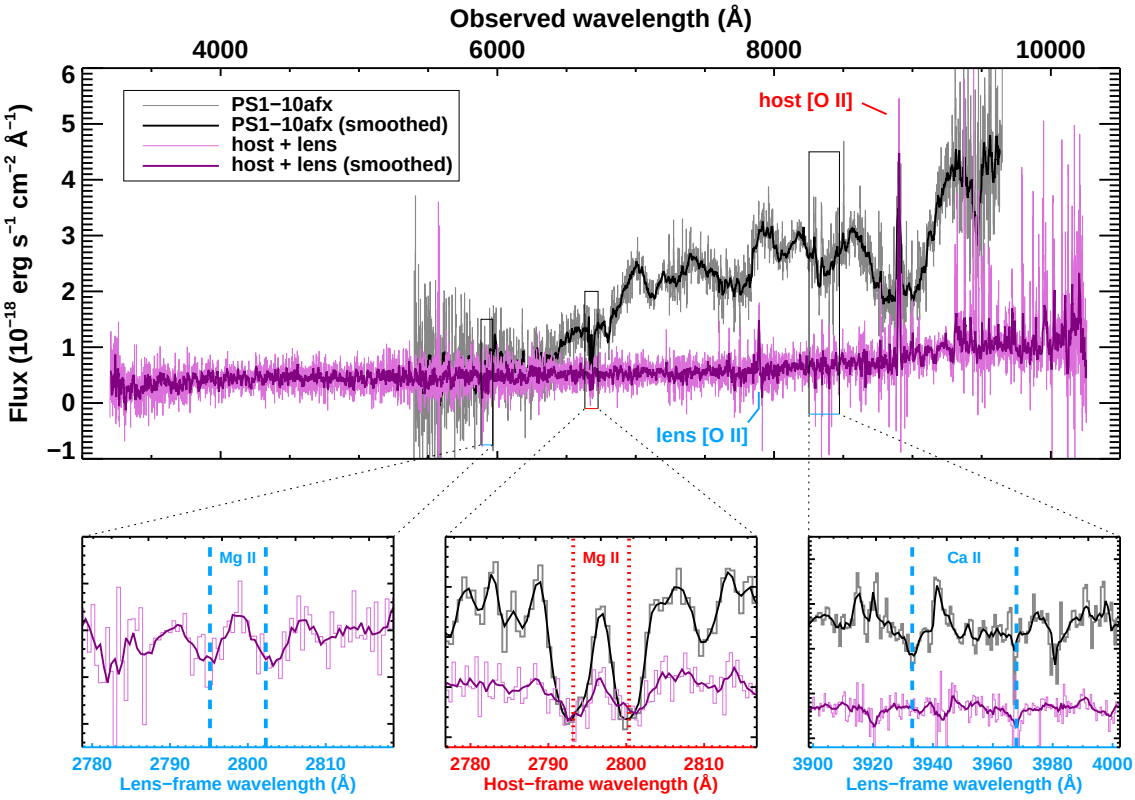

Figure 1: **Spectra of the quiescent light at the location of PS1-10afx.** The Keck/LRIS observations (purple) taken about 450 rest frame days after the supernova reached maximum light show the presence of two emission features, which we identified as [O II] from galaxies at $z = 1.1168$ and $z = 1.3885$. We also detected absorption lines corresponding the Mg II doublet for both the foreground lens galaxy (lower left panel; blue labels) and the host (lower middle panel; red labels). Vertical lines mark the rest frame wavelengths for the doublets in the lower panels. A spectrum of PS1-10afx taken near maximum light (*1*) is shown in gray for comparison. This supernova spectrum has been shifted slightly to align the Mg II features with the Keck/LRIS data (*16*). The lower-right panel shows that the supernova light may be absorbed at wavelengths corresponding to Ca II H&K in the foreground galaxy. Ca II H is coincident with a strong night sky line, but the Ca II K falls in a relatively clean spectral region.

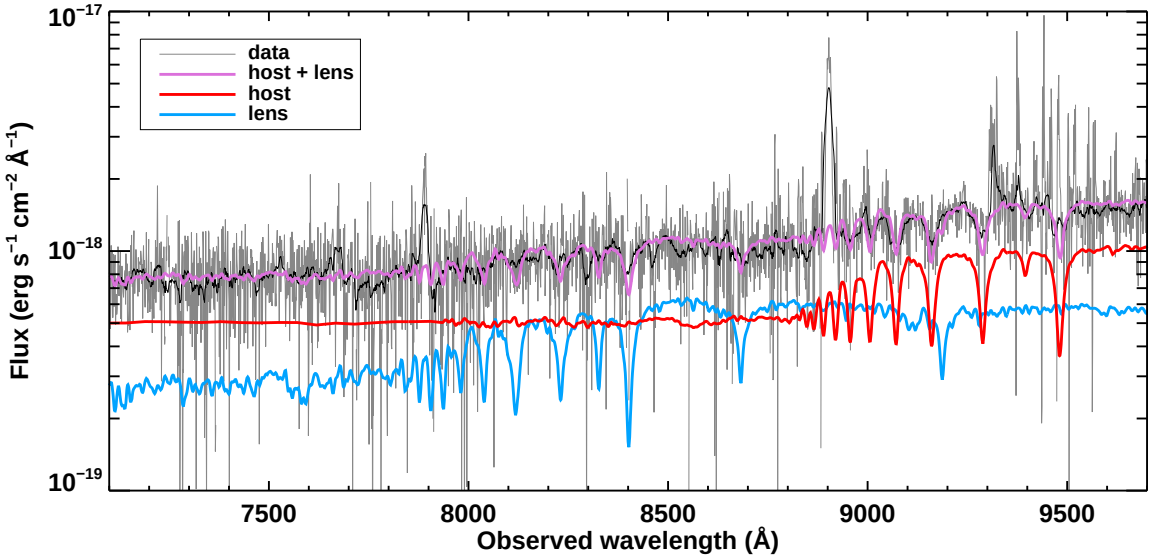

Figure 2: **Decomposition of the observed spectra into lens and host galaxy components.** We modeled the lens (blue line) and host (red line) as single stellar populations at $z = 1.1168$ and $z = 1.3885$, respectively. We varied the age and total stellar mass of each galaxy in order to find the sum (purple line) that best matched the observed spectra (gray; smoothed spectra in black). The models only include starlight; light emitted by gas, such as the [O II] lines seen at about 8900 Å and 7900 Å, is neglected.

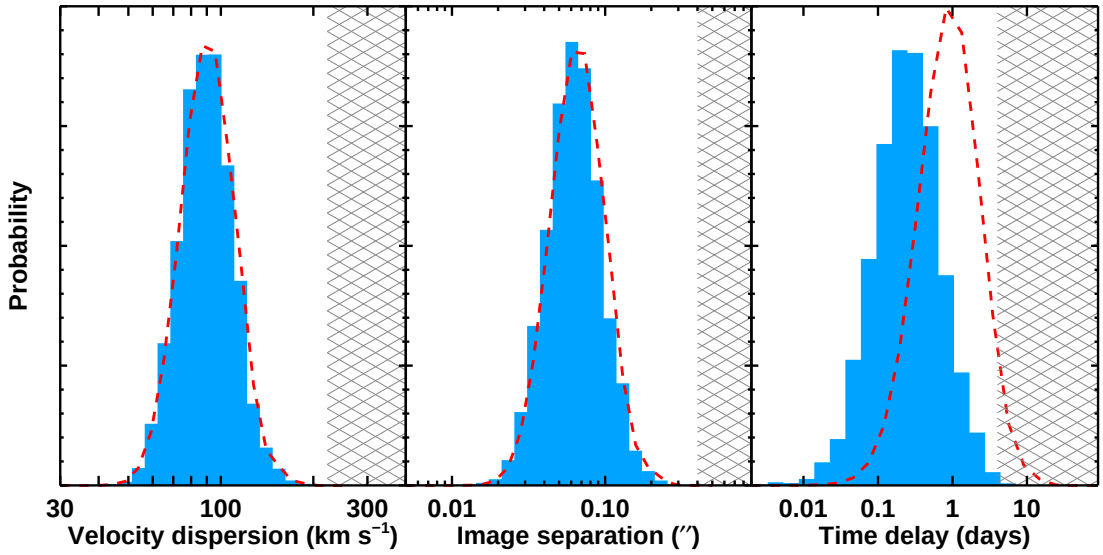

Figure 3: **Probability distributions for the lens parameters.** The panels show, left to right, the relative likelihood for the line of sight velocity dispersion of the lensing galaxy, the maximum separation between lensed images, and the maximum time delay between lensed images as predicted by our Monte Carlo simulation. The blue histograms account for the total magnification, $\mu = 31 \pm 5$, measured for PS1-10afx (*10*), and the dashed red curves neglect this prior. The hatched areas are excluded based on the observations of PS1-10afx, specifically the lack of resolved images or evidence for time delays.

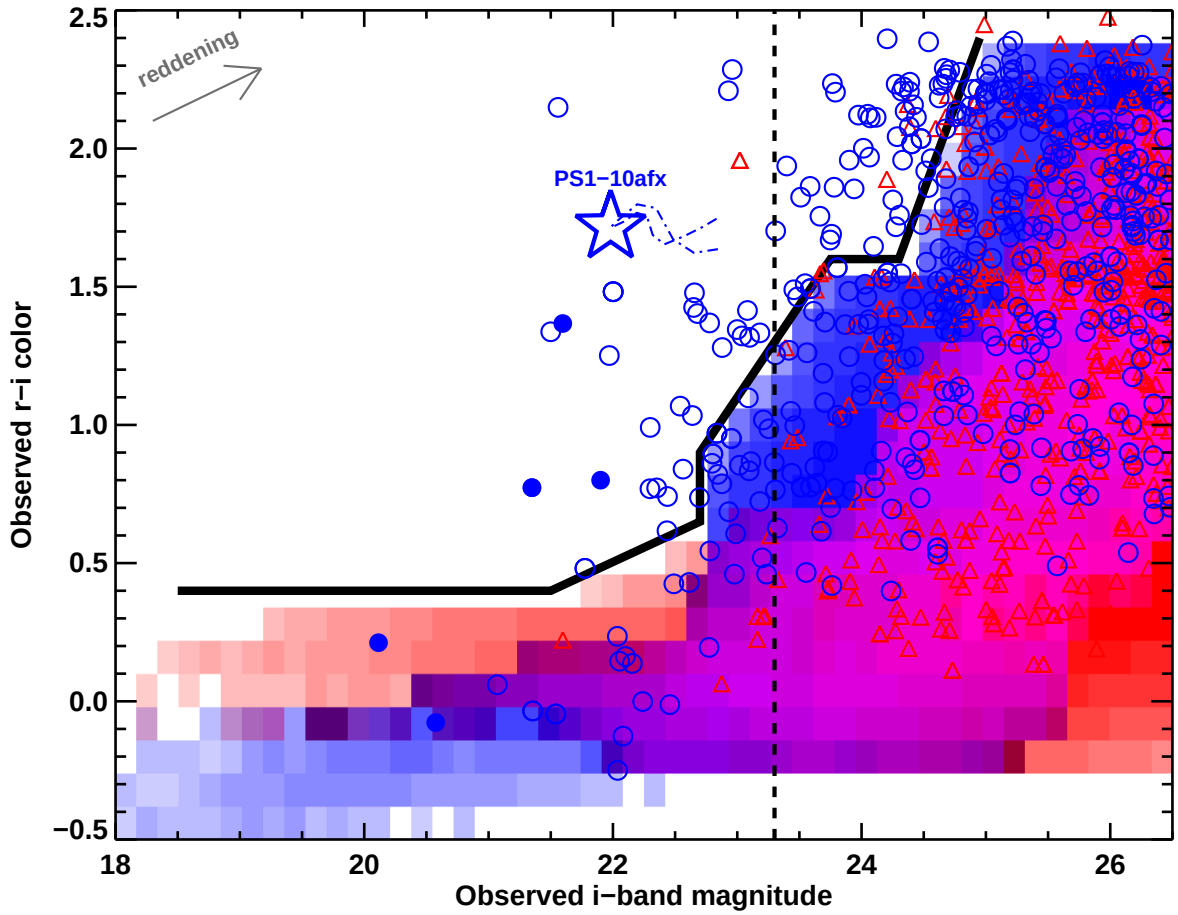

Figure 4: **Color-magnitude diagram showing how lensed SNIa can be distinguished from un-lensed events.** The blue shaded area shows the expected color-magnitude distribution for un-lensed SNIa on a log scale, and the red shaded area corresponds to core-collapse supernovae. The $r - i$ colors for low redshift supernovae are relatively blue. However, at higher redshifts (fainter observed magnitudes), the color becomes red as the peak of the rest-frame spectral energy distribution passes through the observer-frame bands. The red limit for un-lensed supernovae at a given i-band magnitude is denoted by the thick black line. Blue circles and red triangles show the distribution of lensed SNIa and core-collapse supernovae, respectively, predicted by Monte Carlo simulations (*16*). Filled symbols indicate objects that could be resolved from ground based observations, such as those planned by the Large Synoptic Survey Telescope (LSST). Open symbols depict objects that require high angular resolution follow-up observations to resolve spatially. The open star marks the values corresponding to the peak i-band brightness of PS1-10afx, and the dash-dotted curve shows that the color evolution within one magnitude of this peak is minimal. The vertical dashed line marks the single epoch limit predicted for LSST. The arrow shows the reddening vector, assuming $A_V = 1.0$ mag.

Supplementary Materials for

Detection of the Gravitational Lens Magnifying a Type Ia Supernova

Robert M. Quimby,* Masamune Oguri, Anupreeta More, Surhud More,
Takashi J. Moriya, Marcus C. Werner, Masayuki Tanaka, Gaston Folatelli,
Melina C. Bersten, Keiichi Maeda, Ken'ichi Nomoto

*To whom correspondence should be addressed; E-mail: robert.quimby@ipmu.jp.

This PDF file includes:

Supplementary Text

Spectroscopy

The 2013 September 7 observations from the Keck-I telescope with the Low-Resolution Imaging Spectrograph (LRIS) (*17*) employed an atmospheric dispersion corrector to prevent wavelength dependent losses for the non-parallactic slit angles required (*24*). The $1.0''$ slit was oriented to include a nearby star (see Fig. S1), and the telescope was nodded $\pm 2''$ along the slit in an ABBA pattern in several sets over the observation. Light was sorted into red and blue channels using the 560 dichroic. We used the 400/3400 grism for the blue channel, giving a spectral resolution, $R = \lambda/\lambda_{\rm FWHM}$, of about $500 - 700$ from 3200 Å to 5600 Å as measured from arc lamp lines. On the red side, we used the 400/8500 grating to give a spectral resolution of about $1000 - 1700$ between 5600 Å and 10300 Å. The resolution was determined by noting the FWHM of the Gaussian kernel that can best convolve a high resolution night sky spectrum (*25*) to match the sky lines in our data. We used spatial binning on the red channel to give a $0.27''$ pixel^{-1} scale, but left the blue side un-binned ($0.135''$ pixel^{-1}). Integration times were set to 847 s in the blue channel and 817 s in the red channel (per exposure) to accommodate differences in readout speed. A total of 28 exposures (about 6.5 hours on target) were obtained in each channel under good sky conditions and $\sim 0.7''$ seeing.

Two of the blue spectra were found to be anomalous; although the sky counts are similar to the other exposures in the blue, there is a pivot point at longer wavelengths beyond which the counts taper off significantly. These exposures were excluded from our analysis. No problems were found with the associated red channel exposures, suggesting the problem is internal to the blue side of the instrument.

At the end of our first 4 ABBA sets on PS1-10afx, we imaged the slit and found that the

reference star (and thus the position of PS1-10afx) was slightly offset (about 0.4″ West) from the center of the slit. We imaged the slit prior to and after the final 3 ABBA sets to ensure and verify that the slit was properly aligned. The first 4 and second 3 sets are offset along the slit by about 2″, thus placing the target at 4 distinct positions in the detector plane.

We extracted the spectra using IRAF (*26*), called through python scripts using the PyRAF package, for basic de-trending and custom IDL scripts for the final target extraction. We observed the standard star, BD+28d4211, before, in the middle of, and after the PS1-10afx observation for use in spectrophotometric calibration and as a reference for removing telluric features. To correct for atmospheric extinction, we used the Mauna Kea extinction curve (*27*). LA-Cosmic (*28*) was used to mark pixels affected by cosmic rays and particle events on individual frames. We have implemented a 2-D sky subtraction procedure (*29*). Briefly, the sky is fit with B-splines to the two dimensional spectra, with masking and iteration used to exclude object or otherwise deviant pixels. We reduce the data to a 1-D spectrum using optimal extraction applied to the full data set, without ever warping the 2-D spectra. For some of our analysis, we directly use the set of 2-D spectra. The wavelength scale was calibrated first using afternoon arc lamp exposures, and then adjusted by cross-correlating to the UVES night sky spectra (*25*). By cross-correlating sections of our final sky spectrum against the UVES templates, we estimate the corrected wavelengths are accurate to 0.4 Å in the blue channel ($\lambda < 5600$) and accurate to 0.2 Å in the red channel. Finally, we apply a small ($-5\,\mathrm{km\,s^{-1}}$) correction to place the measured wavelengths into the Heliocentric rest frame (this frame differs from the CMB rest frame by about $-350\,\mathrm{km\,s^{-1}}$).

Figures S2 and S3 show the combined 2-D data from the second (properly aligned) pointing near the location of the two emission lines. The spatial coordinate has been set by assuming a separation of 19.13″ between PS1-10afx and the reference star in the slit (see Fig. S1). This coordinate system is only approximate given the uncertainties in the centroid of PS1-10afx

($\sim$0.1″) (*1*), the systematic offset to the CFHT coordinate system (assumed to be $\sim$0.1″), and non-linearities in the Keck/LRIS detector plane (est. $\sim$0.1″). The spatial location of the host, delineated by the extent of the emission line in figure S2, is thus consistent if not slightly south of PS1-10afx. Similarly, the spatial extent of [O II] from the foreground object (Fig. S3) overlaps the location of PS1-10afx and appears to have its centroid some 0.5″ north of the host's [O II], which further suggests these represent physically distinct sources.

For the host galaxy, we derive a redshift of $z = 1.3885 \pm 0.0001$ from the [O II] doublet by fitting a 2-D model to the set of individual exposures. We note that this redshift may be slightly higher than previously reported (*1*). This systematic difference could be caused by calibration differences (e.g. sky lines in the supernova spectra appear systematically offset in wavelength by about 1.6 Å compared to the UVES night sky atlas). Figure S2 suggests a second possibility. The host's [O II] doublet appears to shift in velocity with spatial position. In other words, the galaxy may be rotating and different slit orientations may thus lead to slightly biased redshift measurements (we similarly find a systematic offset between our measurements of the Mg II absorption line wavelengths and those previously reported).

By using the 2-D data to fit for the emission line, we can account for the velocity gradient, which we found to be $127 \pm 25\,\mathrm{km^{-1}\,s^{-1}\,arcsec^{-1}}$ along the slit. Assuming this tilt, the [O II] doublet is resolved, but the individual line widths are consistent with the instrumental resolution. We measured a total [O II] flux from the host light in the slit of $(4.79 \pm 0.05) \times 10^{-17}\,\mathrm{erg\,s^{-1}\,cm^{-2}}$, which is consistent with the value previously reported (*1*). With respect to the [O II] lines, we found that the Mg II absorption lines are blueshifted by $234 \pm 78 \pm 14\,\mathrm{km\,s^{-1}}$, where the first and second errors include only the uncertainty in the absorption minima and only the uncertainty in the [O II] maximum, respectively. This is a higher value than previously reported, but, based on our analysis, we derived a consistent value from the published supernova spectrum ($202 \pm 13 \pm 107\,\mathrm{km\,s^{-1}}$). This blueshift is larger than measured for most star-forming

galaxies observed at $z \sim 1.5$ (*19*), but the sample of such objects with blueshift measurements is small and shows a large scatter (the outflow velocity measured for PS1-10afx's host is less than a standard deviation larger than the sample mean).

For the foreground galaxy, the best fit emission line model prefers a slight dependence on velocity with position, but this is not significant. The total [O II] flux from the foreground galaxy light in the slit is $(1.48 \pm 0.08) \times 10^{-17}$ erg cm^{-2} s^{-1}. From the initial, slightly offset pointing the measured flux is about 50% lower, which suggests the East-West extent of the object is limited.

We note that [O II] emission from the foreground galaxy is not significantly detected in the published spectra of PS1-10afx obtained near the supernova's peak brightness (*1*). If the emitting region was fully contained in the slit aperture, a weak detection of the [O II] line could have been possible. This earlier spectrum was, however, probably optimized for the extraction of the supernova signal and may therefore only contain a fraction of the extended foreground galaxy's light. Considering this, the lower signal-to-noise ratio of the supernova spectrum, and the coincident location of the [O II] line with the blue edge of a broader supernova bump, it is not surprising that the [O II] line was not previously identified.

Stellar Mass Estimates

To test whether the foreground galaxy can satisfy the lensing constraints for PS1-10afx, we must estimate its total mass. A galaxy's rotation curve can be used to estimate a total mass (*30*), so we attempted to fit a 2-D model to the [O II] emission line in the observed spectrum (see section above). However, we do not detect a significant dependence on the emission line's central wavelength as a function of position. Doppler broadening of the absorption lines could also indicate the foreground galaxy's mass (*31*), but the data are confused with the light of the

more distant host galaxy, and the signal-to-noise ratio available from the narrow strip outside of the host's glare is prohibitively low. The Mg II lines noted above are not resolved, which suggests a 1-D velocity dispersion of less than about $\sigma < 90\,\mathrm{km\,s^{-1}}$; yet, if they form in an outflow, the widths of these lines may be decoupled from the galaxy's dynamical mass.

We instead use the foreground galaxy's stellar mass, which is correlated with its 1-D velocity dispersion. We estimate stellar masses for the galaxies by fitting the Bruzual & Charlot (2003) Single Stellar Population (SSP) models (*32*) to our data. We choose models following the Padova 1994 evolutionary tracks, and we tested both Salpeter and Chabrier stellar initial mass functions (IMF). We assume our spectra are composed of two galaxies – one at $z = 1.3885$ and the other at $z = 1.1168$ – each with its own internal extinction. The observed spectra are then modeled as a linear combination of a subset of the models with ages between 0.1 and 5 Gyr. Initially, we assumed each galaxy could be modeled by a bursty star formation history and we allowed each to be comprised of SSP models at four distinct ages all with 0.4 solar metallicity. However, our fits suggest that each galaxy can be well represented by a single age population. We then allowed each galaxy to have any single stellar age in the $0.1 - 5$ Gyr range and metallicities of 0.2, 0.4, or 1.0 solar. We find that young ages ($\sim$0.1 Gyr) are strongly preferred for the Host galaxy, and the foreground galaxy component is best fit with ages close to 1 Gyr.

To account for slit losses, we scaled our spectra by a factor of 1.4 to match the z_{P1}-band magnitude reported for the "host" (*1*). As we have shown, this measurement must actually be a combination of the light from the host and a foreground galaxy. Thus, this scaling may not be perfectly valid for one or both of the galaxies, but the significance of this effect should be small, as noted below.

Assuming the Chabrier IMF, the best fit stellar masses are $(9 \pm 2) \times 10^9\,\mathrm{M_\odot}$ for the foreground lens and $(7 \pm 1) \times 10^9\,\mathrm{M_\odot}$ for the more distant host. The metallicities for the best fit

models are 0.2 solar for the lens and 0.4 solar for the host. These fits are slightly preferred to those with the Salpeter IMF, which gives higher but consistent mass estimates: $(13\pm3)\times10^9\,\mathrm{M}_\odot$ for the lens and $(10 \pm 1) \times 10^9\,\mathrm{M}_\odot$ for the host.

It should be noted that our spectra have relatively less flux below 7000 Å as compared to the "host" colors reported (*1*). If we artificially de-redden our spectra assuming E(B-V) = 0.3, we can recover these colors to within the errors. However, these colors are not compatible with the measurements from the CFHT Legacy Survey (*33*), which, in particular, favor significantly fainter g-band magnitudes for the host. It is thus possible that the integrated color varies with the size and location of the aperture, with the bluer light located outside of our slit (although our two offset pointings show similar colors). Even with this adjustment, however, the derived galaxy masses only change at the $1-2\sigma$ level. If we, instead, normalize the photometry using the reported g-band measurement (*1*), the galaxy masses increase by less than a factor of 2. If the color discrepancy between our spectra and the previous photometry is related to the fractions of the light contributed to by the host and the lens, then this suggests that any error in lens mass due to improperly scaling the light in the slit to the total light measured from the photometry should also be around a factor of 2 or less. Scaled to the g-band photometry, the JHK magnitudes predicted by the best fit SSP models would, like the redder optical bands, be well in excess of the observed constraints. The predicted IR magnitudes are in the best agreement with the observations (all within 1σ) for the z-band scaled case with no artificial reddening correction.

Higher masses for the foreground galaxy are possible if we assume an older stellar population, but these produce worse fits to the data. For example, if we assume a 5 Gyr old population (close to the maximum allowed for a $z = 1.1168$ object), the mass increases to $50 \times 10^9\mathrm{M}_\odot$, but the Ca II K line, which lies in a relatively clean spectral range, would be much stronger in the model than allowed by the data.

If we instead adopt a younger stellar population for the foreground galaxy, then a large

extinction is required. In this case, we would expect the foreground galaxy to redden the light from PS1-10afx, but as previously noted (*10*), the observed colors suggest no extinction of the supernova light. This problem could be avoided by adopting an older age for the host's stellar population, but older SSP models do not match the hydrogen Balmer absorption lines seen in the break in the sky lines between 9000 and 9300 Å (as shown in Fig. 2, we clearly detect H9 and H10 from the host including both broadened absorption dips from the stars and narrow emission lines from gas).

The strongest stellar features expected from the lens galaxy are the hydrogen Balmer and Ca II H & K lines. The signal-to-noise ratio in this wavelength range is lower than in the range covering the host features noted above, and the lens features are expected to be weaker. As shown in figure S4, there is a possible detection of H8, which lies in a relatively clean wavelength range. The simple absorption dip predicted by the SSP modeling could be complicated by nebular emission lines, which are not included in the model. The data in the wings of the H8 feature appear consistent with the SSP model, and there could be a narrow emission feature emerging from the core of the line that would be consistent with nebular light. A similar trend may hold for Hδ and the Hϵ/Ca II H blend, but interference from bright sky lines precludes a definitive conclusion.

Lens Constraints

We derive expected lens properties of PS1-10afx using a Monte Carlo approach (*15*). We first convert our best stellar mass estimate of $M_* = (9 \pm 2) \times 10^9\,\mathrm{M}_\odot$ for the lensing galaxy to a velocity dispersion, σ. Using `linmix_err.pro` (*34*), we find the best fit linear relation to the stellar masses and velocity dispersions of SDSS galaxies (*20,21*) is $\log \sigma = -1.4 + 0.33 \log M_*$, with an intrinsic scatter of 0.081 (see Fig. S5). Propagating the error from the stellar mass es-

timate, we thus adopt a Gaussian distribution with a mean of 1.880 and dispersion of 0.088 for $\log(\sigma[\mathrm{km\,s^{-1}}])$ for the lensing galaxy. We assume the standard singular isothermal ellipsoid mass distribution for the lens with an additional contribution to the lens potential from external shear. The ellipticity is Gaussian distributed with a mean of 0.25 and dispersion of 0.2, and the magnitude of external shear follows a log-normal distribution with a mean of 0.05 and dispersion of 0.2 dex. The position angles are assumed to be random. Fixing the lens redshift to $z = 1.1168$, we randomly generate a list of lenses according to these probability distributions of the velocity dispersion, ellipticity, and external shear. For each lens, we uniformly distribute point sources at $z = 1.3885$, solve the lens equation using the public software, `glafic` (*35*), and record any events that produce multiple images. For all lenses we use the same angular number density of sources, which suggests that the output catalog of multiple images is automatically weighted by strong lensing cross sections.

With this procedure we generate mock catalog of over 500000 multiple image sets. We then derive posterior distributions of any parameter X directly (e.g. the dashed red lines in Fig. 3) or, for a consistency check with PS1-10afx, by adding a condition on the total magnification μ, $P(X) = \int P(X|\mu)P(\mu)d\mu$ (the blue histograms in Fig. 3), where $P(\mu)$ is assumed to be Gaussian distribution with a mean of 31 and dispersion of 5, which corresponds to the best-fit and error of the total magnification of PS1-10afx (*10*). When so weighted by the lensing probability, the velocity dispersion for the lensing galaxy is found to be $\log(\sigma) = 1.95 \pm 0.09$, the image separation is $\log(\Delta\theta) = -1.20 \pm 0.18$ (with $\Delta\theta$ in arcseconds), and the time delay is $\log(\Delta t) = -0.61 \pm 0.44$ (with Δt in days). We also find that the centroid of the combined supernova images should be offset from the lens center by $\log(\theta) = -1.68 \pm 0.26$ (with θ in arcseconds).

These values are fully consistent with the observations of PS1-10afx. To be inconsistent, the velocity dispersion would have to be significantly larger than we have estimated. If we adopt

the velocity dispersion implied by the highest stellar mass considered above ($50 \times 10^9 M_\odot$ or $\log(\sigma) = 2.13$), for example, the expected lens parameters would still be consistent with the observations of PS1-10afx. This strengthens our conclusion that the foreground galaxy is the gravitational lens that has magnified PS1-10afx.

We perform an additional plausibility check that is completely independent of our stellar mass estimate. We consider the probability distribution of the 1-D velocity dispersion of galaxies at $z = 1.1168$ that can act as a lens for a $z = 1.3883$ source. For a spherically symmetric gravitational lens with an isothermal density profile characterized by a velocity dispersion σ, the Einstein radius is given by,

$$b = 4\pi \left(\frac{\sigma}{c}\right)^2 \frac{D_{\rm ls}}{D_{\rm s}}, \tag{1}$$

where $D_{\rm ls}$ and $D_{\rm s}$ are angular diameter distances from lens to the source and from observer to the source, respectively. The lens cross-section for a spherical isothermal model is given by $\mathcal{A}_{\rm lens} = \pi b^2 \propto \sigma^4$. Therefore, the probability distribution of the velocity dispersion of a galaxy at redshift $z_{\rm l}$ to lens a background galaxy at redshift $z_{\rm s}$ is given by

$$P(\sigma|z_{\rm l}, z_{\rm s}) \propto n(\sigma, z_{\rm l})\mathcal{A}_{\rm lens} \propto n(\sigma, z_{\rm l})\sigma^4 . \tag{2}$$

We use the inferred velocity dispersion function for the sample of galaxies in the redshift range $0.9 \leq z \leq 1.2$ (*36*). We fit a Schechter function to these data points, and extrapolate the resulting velocity dispersion function to lower values of the velocity dispersion. The probability distribution function for the lens velocity dispersion is then obtained by inserting this velocity dispersion function into Equation 2. We have restricted ourselves to those velocity dispersions which result in image separation distribution less than $0.4''$, given that PS1-10afx was not resolved by Pan-STARRS imaging data. The angular size of the SN photosphere must be smaller than the SN$-$lens angular offset, $\Delta\theta$, to avoid changes in the effective magnification over time. This puts a constraint on the lower mass end of the velocity dispersion. After the application of

these priors, the median velocity dispersion, $\sigma = 177^{+32}_{-47}$ km s^{-1}, is compatible if not slightly higher than the value derived through our Monte Carlo simulation. This value is also consistent (albeit at the higher end) of the $\sigma - M_*$ relation derived from the SDSS galaxies, which is not entirely unexpected given that lensing probability grows rapidly as σ increases (Eqn. 2).

Selecting Lensed SNIa in Color-Magnitude Space

To determine the distribution of lensed and un-lensed supernovae in color-magnitude space, we first calculate the observed magnitudes expected in the r and i-bands for SNIa and core-collapse supernovae as a function of redshift. For band X, the observed magnitude is computed from $m_X = M + \mu + K_X$, where μ is the distance modulus, M is the absolute magnitude of the supernova in some rest frame band, and the K_X term accounts for the offset between this band and band X including the effects of redshift. We allow for a range of peak absolute magnitudes for each type of supernova (*37*). We calculate the so-called K-corrections using spectral energy distribution templates for various supernovae (*38, 39*). We use the rates of supernovae (*40*) to determine the relative numbers of each type of supernovae with redshift.

The sample of supernovae generated from this is then used as input to a Monte Carlo simulation that determines what fraction of events are lensed and by how much. For the lensing galaxies, we adopt the velocity function measured from SDSS galaxies (*41*). We assume no redshift evolution. The strong lensing probability is calculated assuming a singular isothermal ellipsoid with a fixed ellipticity of 0.3. For each lensing event, the total magnification is computed using `glafic` (*35*). With the updated velocity function and ellipticity, we find the lensing probability is a factor of 2 higher than previously published (*15*). Our simulations show that for a flux limited survey, the $r - i$ colors of most lensed supernovae can be significantly larger (redder) than the un-lensed events. Objects found to lie above the bold line in figure 4

can thus be considered lensed supernova candidates.

We can verify the purity of such selection criteria using the published sample of supernova discoveries from the Supernova Legacy Survey (SNLS) (*42*). Unfortunately, only the set of well characterized events (e.g. SNIa) is available but we can at least use these to verify that the dominant product of similar supernovae surveys will be excluded from our selection cuts. The filters used in the SNLS Survey differ slightly from the standard SDSS band passes, which leads to slightly different selection criteria than depicted in figure 4. Accounting for this, we compare the observed i-band magnitudes and $r - i$ colors of the SNLS sample and find that all events detected before maximum light have photometry that lies below our selection line at some point before declining. At late times, the colors can be redder, but selecting only those objects that are consistently above our (appropriately modified) selection line during their rise to maximum light eliminates the entire SNLS sample. The selection criteria thus succeeds in weeding out normal supernovae during their rising phase and enables the selection of lensed SNIa on the rise, which will enable good constraints on the date of and flux at maximum light.

Selection Bias and the Expected Number of Lensed SNIa from Pan-STARRS1

Even though the magnification of PS1-10afx is larger than expected from a random, strong-lensing system in a given volume and the lens galaxy is less massive than a random draw weighted by lensing cross section would predict, the system may well prove typical of the gravitationally lensed SNIa discoveries that will be found by future surveys. Flux limited surveys like Pan-STARRS1 have a strong bias against less magnified SNIa, which are fainter thus harder to detect. Because both lensing optical depth and the number of SNIa is a steep function of redshift (especially around $z \sim 1$) due to increasing comoving volume and, in the case of SNIa, rates, there are more strongly lensed SNIa at higher redshifts with large magnifications than at

lower redshifts with lower magnifications (and thus similar observed magnitudes). There is thus a strong overall bias for highly magnified SNIa. Also, the angular resolution of Pan-STARRS1 is sufficient to resolve lensed SNIa with large image separations, which are necessarily seen through the most massive lens galaxies, but the SN images seen through smaller lens galaxies are more likely to be unresolved. Small lens galaxies thus have a selection advantage in flux limited searches as the multiple supernova images will blend together to form a single point source with a flux equal to the sum of its parts; in the case of resolved images, the individual images must be detected, but these will of course be fainter.

We illustrate this point in figure S6, which shows the distribution of gravitationally lensed SNIa expected to be detected by the Pan-STARRS1 Medium Deep Survey (PS1-MDS). We first used a Monte Carlo simulation similar to one previously published (hereafter OM10) (*15*) to predict the distribution that would be found using prior selection techniques. Specifically, detection of the third brightest image was required for quads and detection of the second image was required for doubles. Excluding unresolved systems, the total number of gravitationally lensed SNIa predicted by this method is 0.1 over the survey lifetime, which is consistent with the number published in OM10. However, if we only require detection of a single image (or a single blend in the case of unresolved images), the expected number of gravitationally lensed SNIa from the PS1-MDS jumps to 0.9. About half of these should be unresolved by the survey, like PS1-10afx. The Monte Carlo simulation further predicts that a SNIa sample selected in this way will have a mean total magnification of 13.0, a median of 5.0, and 95% of the sample will have total magnifications in the range $2.0 < \mu < 59.2$. This, again, is consistent with PS1-10afx.

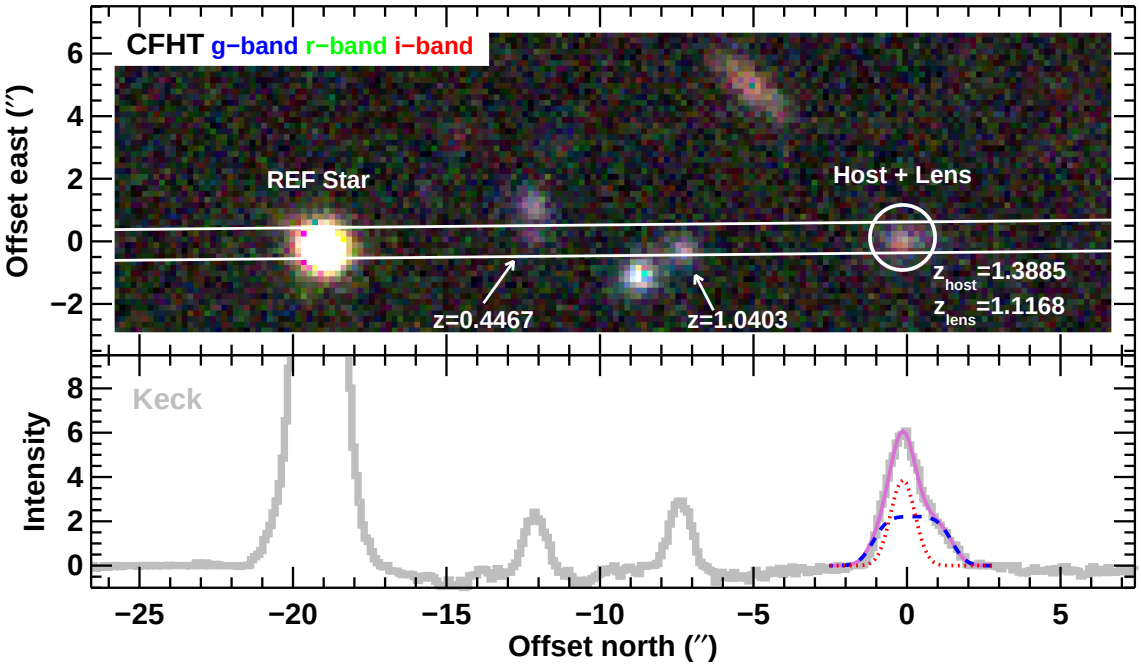

Figure S1: Field setup for the Keck/LRIS observation of PS1-10afx. The top panel shows a color-composite image of the sky near PS1-10afx using g, r, and i-band data taken prior to the outburst by the Canada-France-Hawaii Telescope Legacy Survey (*33*). The lines mark the location of the 1.0″ slit mask deployed for spectroscopy. The location of PS1-10afx is marked with a white circle, and the redshifts of nearby galaxies, as determined from the Keck spectra, are indicated. The lower panel shows the 1-D intensity along the slit as recorded by the Keck observation. The target profile (purple line) was decomposed into a marginally resolved host component (red dotted line) and an extended foreground galaxy component (blue dashed line).

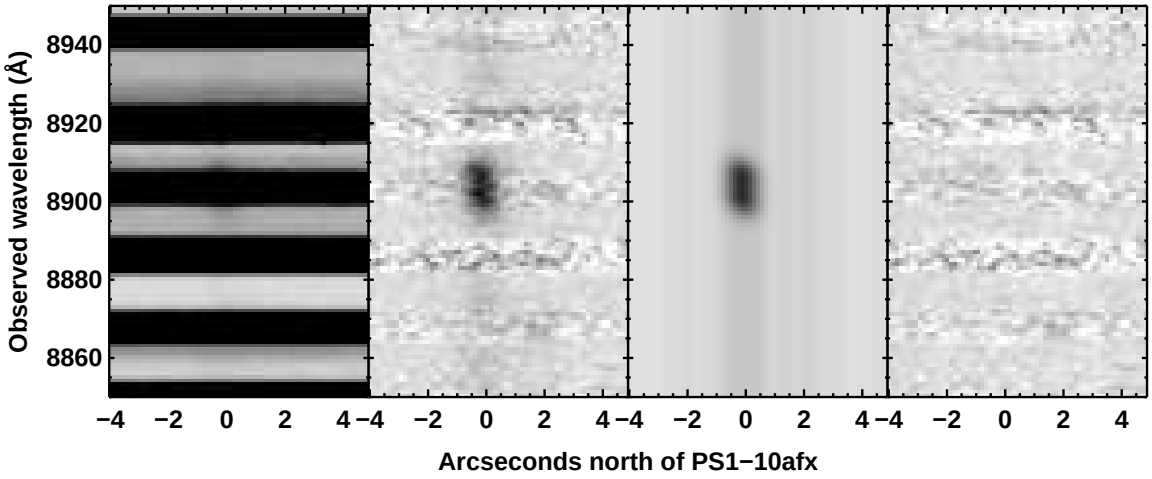

Figure S2: Composite 2-D spectra showing the [O II] emission from the host at $z = 1.3885$. The first two panels on the left show the stacked spectra before and after removal of the sky background. The next panel shows the 2-D model for the emission lines and continuum, and the right panel shows the residual after this model was subtracted from the second panel.

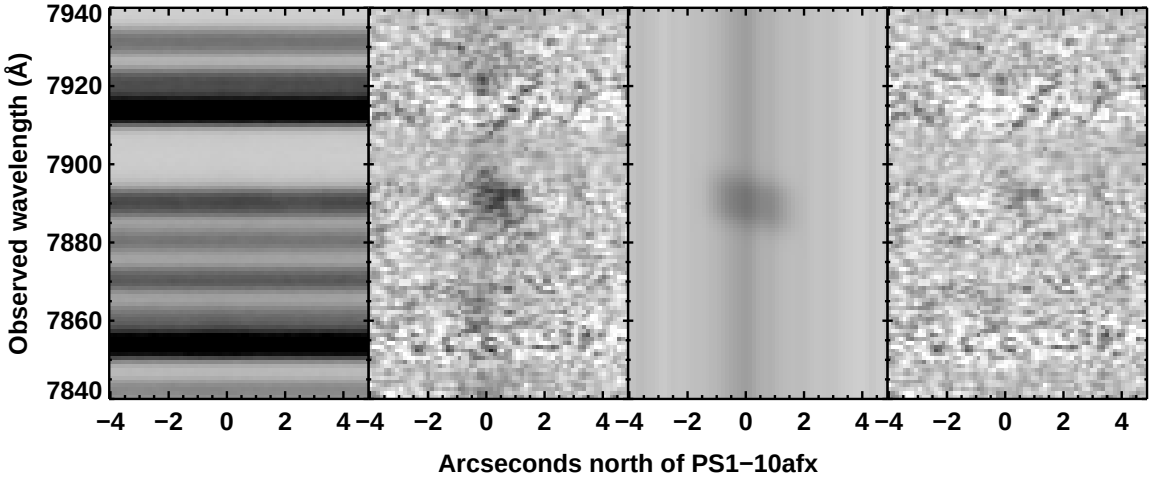

Figure S3: Similar to figure S2 but showing the [O II] emission from the foreground galaxy at $z = 1.1168$.

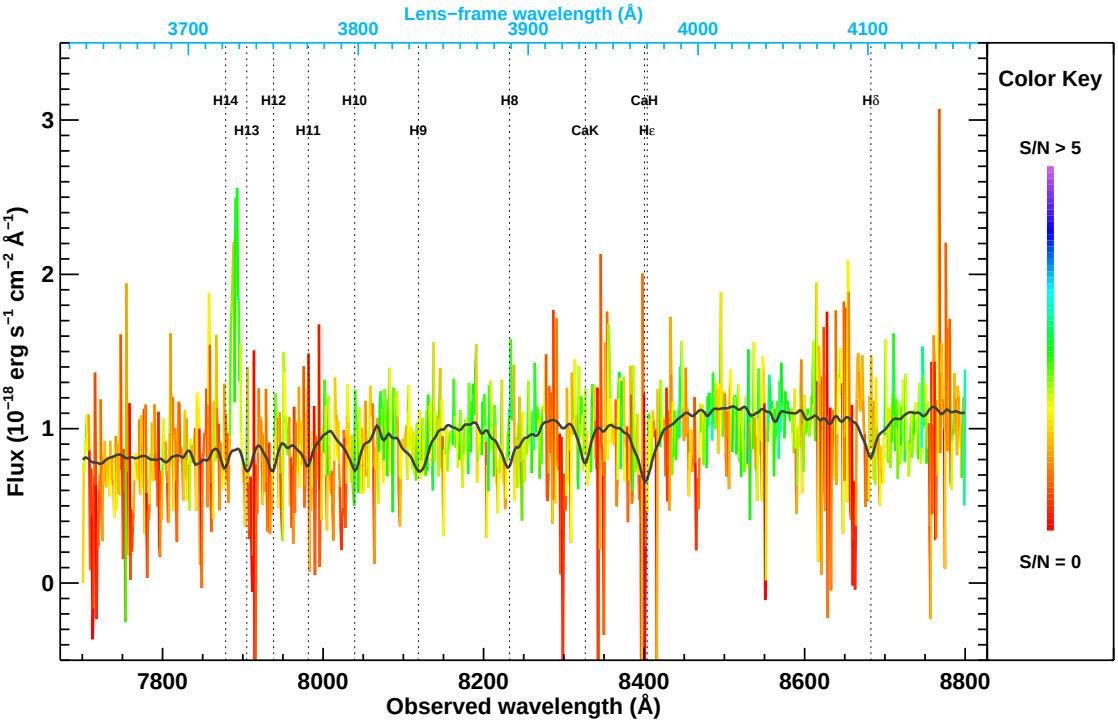

Figure S4: Detail of the best fit SSP model showing the strongest stellar lines expected from the lens galaxy. The data are color coded by the signal-to-noise ratio (per Angstrom) as indicated in the legend. The dark gray curve is the best fit SSP model, which includes the total starlight expected from the host and lens but neglects emission from nebular gas.

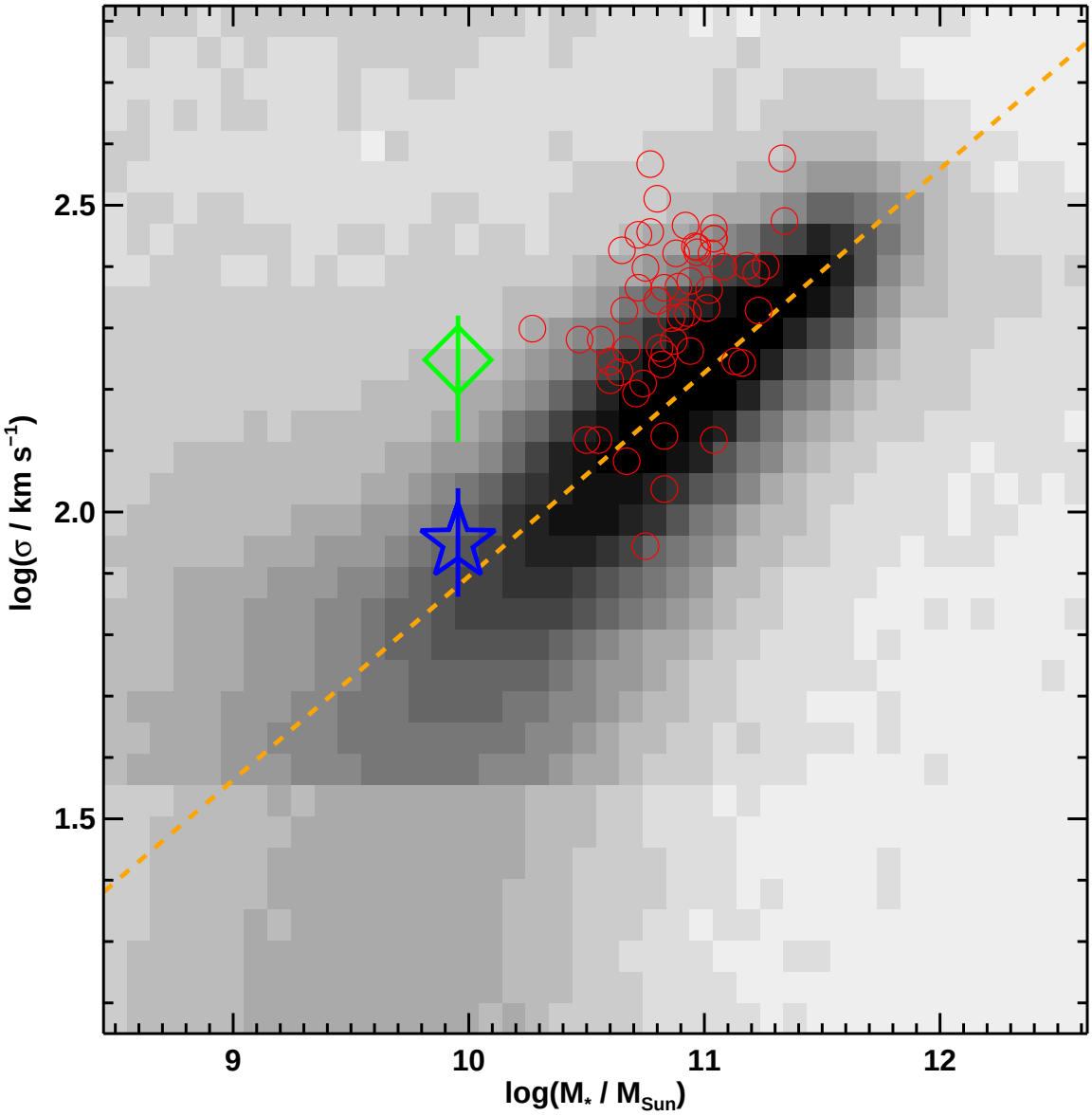

Figure S5: Stellar mass (M_*) vs. velocity dispersion (σ) relation for galaxies. The gray scale contours show the density of galaxies from the SDSS (*20, 21*) on a cube root scale. The dashed orange line shows the best fit linear relation. The blue star marks the most probable σ for the lensing galaxy including the magnification prior from our Monte Carlo simulation, and the green diamond is the estimated value from the analytic calculation. The red circles are for a sample of galaxies at redshifts comparable to the lens (*43*).

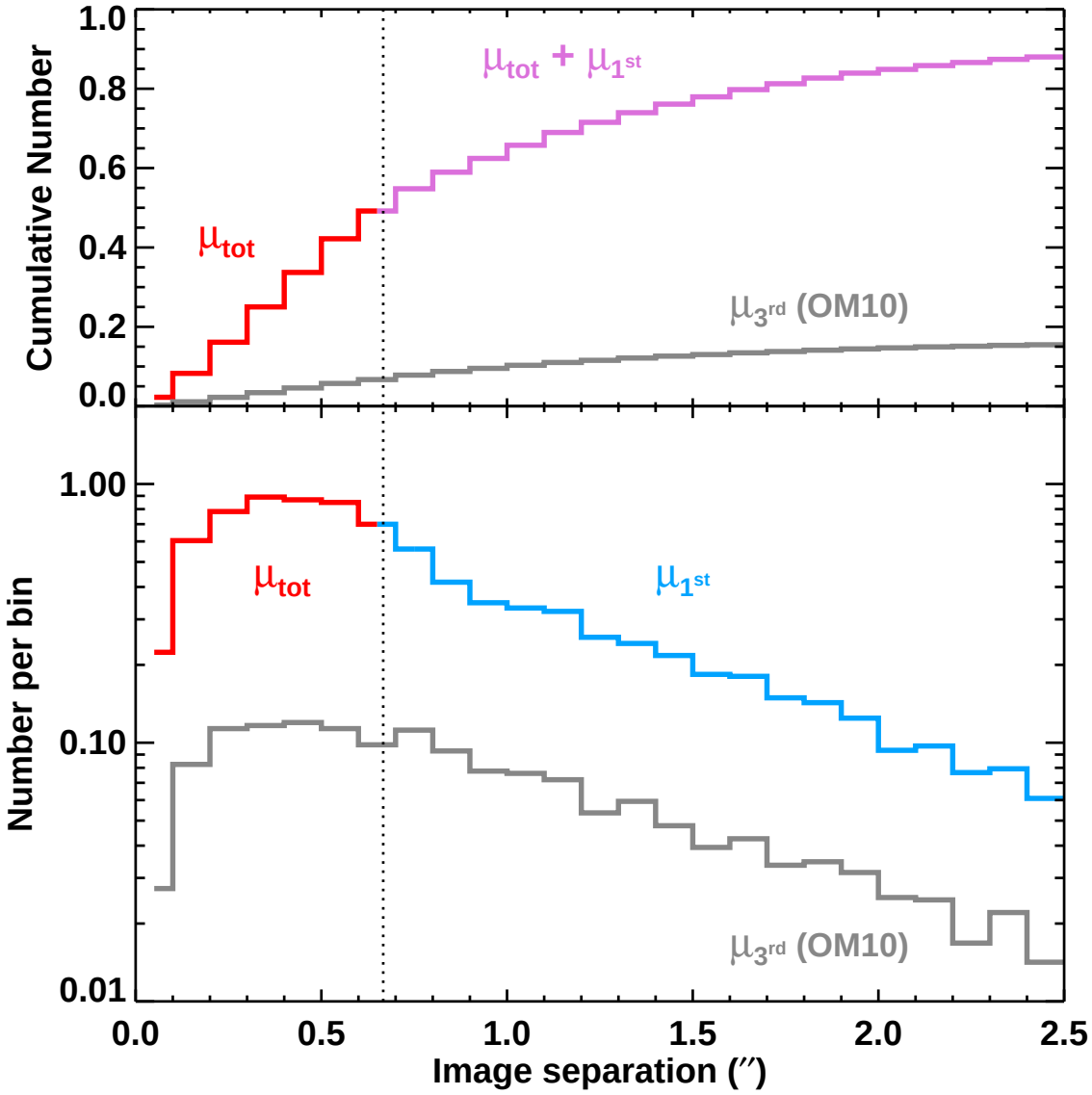

Figure S6: Expected number distribution of lensed SNIa from the PS1-MDS as a function of image separation angle (the distance between the two images in a double or the maximum separation in a quad system). Predictions from OM10 (*15*) were based on the detectability of the fainter image in a double and the third brightest image in a quad (gray lines in the figure). Using the color selection, lensed supernovae can then be identified solely from the brightest image in the system ($\mu_{1^{st}}$; blue line). When the image separation is below the resolving power of the survey (vertical dotted line), the relevant brightness is set by the sum of the individual images (μ_{tot}; red lines). The total number of lensed SNIa detectable by PS1-MDS is then roughly an order of magnitude larger than previously considered.